Voltage X-Ray Reflectometry: A Method to Study Electric-Field-Induced Changes in Interfacial Electronic Structures

Sven Erik Ilse[1], Gisela Schütz,[2] and Eberhard Goering[1,*]

[1]*Max-Planck-Institute for Solid State Research, D-70569 Stuttgart, Germany*
[2]*Max-Planck-Institute for Intelligent Systems, D-70569 Stuttgart, Germany*

Magnetic multilayers with a separating insulating layer are used in a multitude of functional devices. Controlling the magnetic properties of such devices with an electric field has the potential to vastly enhance their performance. Nevertheless, experimental methods to study the origin of electric-field-induced effects on buried interfaces remain elusive. By using element selective x-ray resonant magnetic reflectometry we are able to gain access to changes in the electronic structure of interfacial atoms caused by an electric field. With this method it is possible to probe interfacial states at the Fermi energy. In a multilayer stack with a Ni/SiO_2 interface, we find that the electric field slightly shifts the Ni L_3-edge in energy, which indicates a change of the oxidation state of interfacial Ni atoms. Further analysis of the strength of the effect reveals that only about 30% of the electrons moved by the electric field end up in interfacial Ni states.

In order to understand and engineer electric-field-related effects at interfaces in buried systems such as spintronic tunnel junctions, MOSFETs, capacitors, and multilayered systems including an insulating layer in general, field-induced changes to the electronic structure have to be known. Exploiting electric-field-induced effects such as the voltage control of magnetic anisotropy has the potential to significantly enhance the functionality of spintronic devices [1–4]. Theoretical studies to unravel the underlying physics of the magnetic anisotropy effect are numerous [5–9], with the Bruno model leading the way [10].

However, experimental evidence for those theoretical models still remains mostly elusive, since reliable experimental techniques to study electric-field-induced effects at buried interfaces are rare. First attempts to directly measure electric-field-induced changes to the x-ray absorption spectroscopy (XAS) and x-ray magnetic circular dichroism (XMCD) signal of Fe at the L-edges were carried out by Miwa *et al.* in 2015 [11]. They successfully measured voltage-induced changes to the amplitude of the XMCD signal in Ni, Co, Fe, and Pt thin films at the L-edges of those materials [12–16]. Complete spectra of electric-field-induced changes for 3d transition metals, however, are still lacking.

X-ray reflectometry and x-ray resonant magnetic reflectometry (XRMR) are excellent tools to measure interfacial properties of buried layers [17,18]. X-ray reflectometry and XRMR have been successfully used to retrieve spatially resolved electronic structures and depth dependent orbital polarization profiles of superlattices [19–22], to study pinned magnetic moments [23,24], or to investigate magnetic proximity effects [25–30]. More recently, time dependent measurements have enabled depth dependent magnetization dynamics [31] and depth dependent ultrafast demagnetization measurements [32].

In this Letter we introduce lock-in based voltage x-ray reflectometry (VXRR). This method allows for element specific investigations of electric-field-induced changes in the electronic structure at interfaces in thin layered systems. Hence, this method allows to probe interfacial states at the Fermi energy. For this study, we used a 5×5 mm^2 Si substrate with a 59.3 nm thick thermally grown SiO_2 coating and subsequently sputtered 2.2. nm Ni, 1.4 nm Cr, and 8.6 nm Au on top. The SiO_2 acts as an insulating layer so that the applied electric field accumulates charges at the Ni/SiO_2 interface. A sketch of the sample design with the sign of the applied electric field and the measurement geometry is shown in Fig. 1. A sinusoidal alternating electric field is applied across a multilayer system and the induced change of the resonant reflected x-ray intensity is measured via a lock-in technique. The change of the local electronic structure is then retrieved by fitting the measured reflectivity data with ReMagX [17,18,33].

Reflectivity measurements were carried out with the three-axis ultra-high-vacuum reflectometer ERNSt [34] operated at the UE56-2 PGM-2 beamline at the BESSY II synchrotron in Berlin, Germany. Off-resonant Θ–2Θ scans at multiple energies and resonant scans at the Ni L_3-edge were used to determine the exact chemical
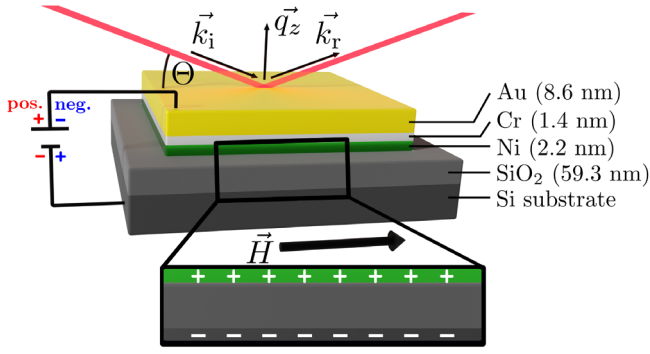
FIG. 1. Sketch of the sample design and measurement geometry. The incoming and reflected x rays are depicted in red with wave vector $\vec{k}_\mathrm{i}$ and $\vec{k}_\mathrm{r}$, respectively; the momentum transfer $\vec{q}_z$ is defined as the difference between $\vec{k}_\mathrm{r}$ and $\vec{k}_\mathrm{i}$. The enlargement depicts a positive applied voltage, where holes accumulate at the $\mathrm{Ni}/\mathrm{SiO}_2$ and electrons at the $\mathrm{SiO}_2/\mathrm{Si}$ interface.
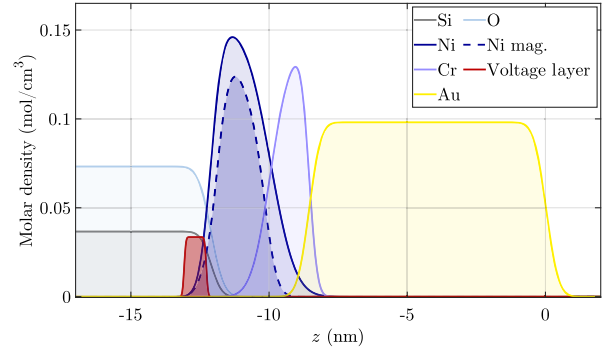

FIG. 2. Elemental and magnetic depth profile of the studied sample. The depth dependent magnetization profile of the Ni layer is shown with the dashed line. Details on how those profiles are determined can be found in the Supplemental Material [35], Sec. II. The layer that is affected by the applied electric field is shown in red. Details about the relation between chemical depth profile and scattering length density can be found in the Supplemental Material [35], Sec. VI.

and magnetic depth profile of the sputtered sample (see Supplemental Material [35], Sec. II). The corresponding structural and magnetic details are presented in Fig. 2. The magnetic depth profile shows that Ni has a slightly reduced bulk magnetization, a strong magnetization reduction at the Cr interface, and an almost full magnetization at the SiO_2 interface. All measurements were performed at room temperature while an in-plane field of 117 mT was applied to saturate the Ni film. Circularly polarized x rays were used to disentangle charge and magnetic contributions from the voltage dependent signal by means of the XMCD effect.

The alternating electric field pushes (pulls) electrons to (from) the interfaces that populate (depopulate) Ni states close to the Fermi energy, respectively. This slightly changes the x-ray optical properties of the Ni interface for energies around the Ni L-edges, resulting in reflected x-ray intensity changes. The intensity variations are in the subpermille range, hence the lock-in technique is necessary. Two measurement modes were used: constant energy and constant q_z scans [17,18]. In constant energy mode, the photon energy is kept fixed and the momentum transfer q_z is swept. In constant q_z mode, the energy and the angle Θ are varied in order to keep the momentum transfer q_z constant. The alternating electric field is applied with a frequency of 59 Hz, which was determined to be the optimal frequency for this particular experimental setup (see Supplemental Material [35], Fig. S1, for details on how the optimal frequency was determined). In our setup a positive (negative) voltage accumulates holes (electrons) at the $\mathrm{Ni}/\mathrm{SiO}_2$ interface, respectively. The resulting voltage asymmetry ratio A_V is calculated via

$$A_\mathrm{V} = \frac{I_{V+} - I_{V-}}{I_{V+} + I_{V-}} = \frac{I_\text{lock-in}}{2I}, \qquad (1)$$

where I_{V+}, and I_{V-} are the reflected x-ray intensities with positive and negative applied voltage, respectively. The difference of these two intensities is the measured lock-in signal $I_\text{lock-in}$ and their sum is the same as 2 times the averaged measured reflected intensity I. The simulation software ReMagX is then used to vary the x-ray optical parameters at the interface in such a way that the simulation matches the measured voltage asymmetry ratio.

In the present study, an ac voltage of 12 $\mathrm{V_{rms}}$ is applied across the layer stack. This results in an effective electric field strength of $E_\mathrm{rms} = 0.2024$ (V/nm). The relative permittivity ϵ_r of the insulating SiO_2 layer can be derived from the measured capacitance $C = (5.21 \pm 0.08)$ nF of the sample and was found to be $\epsilon_r = 3.9 \pm 0.1$, which is in perfect agreement with literature values [37]. With that, the effective displacement field applied to the layer stack can be calculated to be $D_\mathrm{rms} = \epsilon_r\epsilon_0 E = 0.007$ $(\mathrm{C/m^2}) = 4.36 \times 10^{16}$ $(\mathrm{e^-/m^2})$.

Constant energy measurements of the voltage asymmetry were performed at two different energies around the Ni L_3-edge and with the sample magnetization and photon helicity parallel and antiparallel, respectively. Results measured at 849.8 eV, which is just at the onset of the Ni L_3-edge, are presented in Fig. 3, while measurements at 850.5 eV, which is at the maximum of the Ni L_3-edge, are shown in Fig. 4 (see Supplemental Material, Sec. IV, for detail on how the error bars are determined [35]). The amplitude of the voltage asymmetry ratio is smaller than 0.5‰ within the measurement range. The actual measured photocurrent difference $I_{V+} - I_{V-}$ is below 0.5 pA for small q_z and decreases quickly with increasing q_z (for details see Supplemental Material [35], Fig. S3). However, the voltage asymmetry ratio increases with q_z because the total reflected intensity I decreases faster with q_z than the intensity difference. This behavior is similar to magnetic asymmetries measured with XRMR [see, for example,
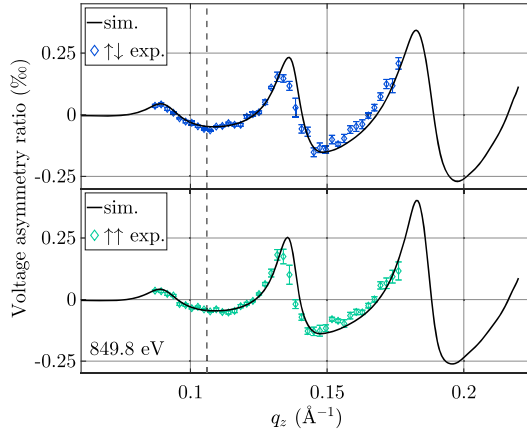
FIG. 3.   Voltage asymmetry ratio measured at the onset of the Ni L_3-edge at 849.8 eV with antiparallel (blue) and parallel (green) configuration of sample magnetization and photon helicity and the corresponding ReMagX fits (black). The dashed line denotes the q_z value where the constant q_z scans were measured.

Figs. S2(b) and 2(c) in the Supplemental Material [35] or [18]]). The voltage asymmetry ratio is higher for the measurement at the onset of the Ni L_3-edge (see Fig. 3), when compared to the measurement at the maximum of the Ni L_3-edge (see Fig. 4). In Fig. 5, constant q_z scans over the Ni L_3-edge at $q_z = 0.106$ Å^{-1} with parallel and antiparallel configuration are presented. The value of $q_z = 0.106$ Å^{-1} was selected since the lock-in measured photocurrent difference is highest at this point (see Fig. S3 in the Supplemental Material [35]). The voltage asymmetry ratio shows a sharp edge for both configurations between 849.0 and 849.8 eV where it increases from zero to -0.05‰. At higher energies, the voltage asymmetry ratio decreases continuously until it returns to zero at 855.0 eV.

The maximum of the measured signal is at 849.8 eV, which is at the onset of the Ni L_3-edge. Measurements on the voltage dependence of the signal are presented in the Supplemental Material [35], Sec. V, and show a linear response.

In order to extract valuable data from the presented voltage asymmetry ratios, reflectivity simulations are necessary. The corresponding resonant x-ray optical properties were therefore retrieved from XAS and XMCD measurements, as shown in Fig. 6 in blue and green [and in Figs. 2(d) and 2(e) in the Supplemental Material [35]]. For further simulation of the voltage asymmetry ratios (both, the q_z and constant q_z scans), an artificial layer at the Ni/SiO$_2$ interface is introduced in ReMagX, which reflects the position of the moved charges induced by the voltage. Similar to the method used for the simulation of magnetic depth profiles [18], the artificial layer only carries the optical properties modified by voltage. The resulting fits, also shown in Figs. 3–5, are in almost perfect agreement with the experimental data. In Fig. 2, the chemical and magnetic depth profiles of the sample are shown. The artificial layer that represents the Ni atoms influenced by the voltage is plotted in red. The position of the layer strongly affects the periodicity of the fit in Figs. 3 and 4, which is why the position can be determined with ± 0.3 nm accuracy (see Fig. S4 in the Supplemental Material [35]). The resulting position of the voltage layer suggests that only Ni atoms closest to the Si substrate are affected by the electric field, as the electric field is highest for those Ni atoms, especially at peak positions. For a quantitative analysis the product of width and density of the layer, which represents the number of Ni atoms per area affected by the electric field N_{Ni}, is chosen to match the area density of an effective Ni monolayer (see below). For a constant width-density product and a voltage layer roughness below the chemical interface roughness the fit does not change
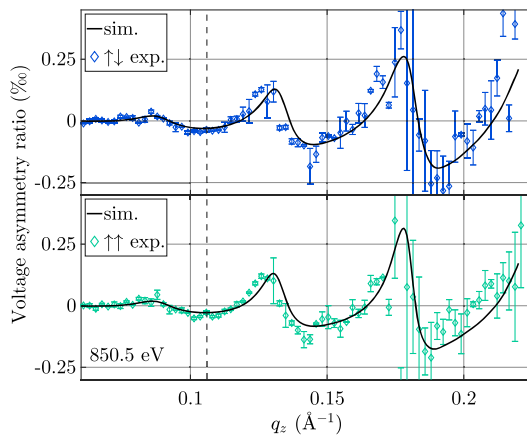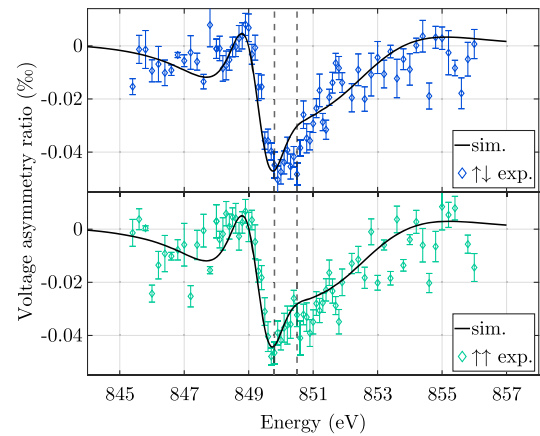

FIG. 4.   Voltage asymmetry ratio measured at the maximum of the Ni L_3-edge at 850.5 eV with antiparallel (blue) and parallel (green) configuration of sample magnetization and photon helicity and the corresponding ReMagX fits (black). The dashed line denotes the q_z value where the constant q_z scans were measured.

FIG. 5.   Constant q_z scan over the Ni L_3-edge at a q_z value of $q_z = 0.106$ Å^{-1} with antiparallel (blue) and parallel (green) configuration of sample magnetization and photon helicity and the corresponding ReMagX fits (black). The dashed lines indicate at which energies constant energy scans were performed.
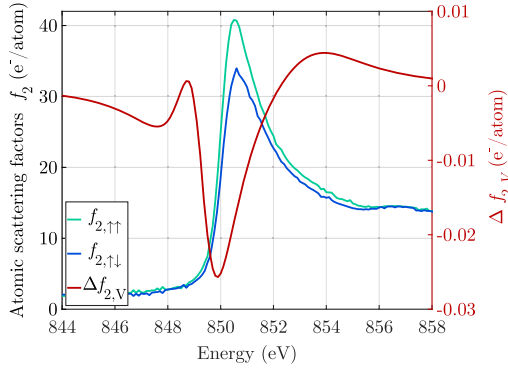
FIG. 6. Imaginary part of the atomic scattering factor f_2 including the magnetic component of Ni at the L_3-edge (blue and green) and $\Delta f_{2,V}$, which corresponds to the XAS difference between positive and negative applied voltage (red).

significantly when changing the width, the density, or the roughness of the voltage layer.

In order to simulate the constant q_z voltage asymmetries voltage x-ray optical properties are introduced, namely $\Delta f_{1,V}$ and $\Delta f_{2,V}$. Those are the voltage dependent analogs of the magnetic components of the x-ray optical properties and are modeled with a superposition of 3 Lorentzian functions. These are added to the atomic scattering factors. $\Delta f_{1,V}$ and $\Delta f_{2,V}$ are analytically connected via Kramers-Kronig relations. The shape and position of the energy dependent voltage x-ray optical properties are varied until the measurements shown in Figs. 3–5 are reproduced by ReMagX fits. The simulation results are shown as black lines, all based on the same voltage x-ray optical properties $\Delta f_{1,V}$ and $\Delta f_{2,V}$. In Fig. 6, the imaginary component $\Delta f_{2,V}$ is shown in red, while the real component $\Delta f_{1,V}$ is retrieved via Kramers-Kronig relations and can be seen in Fig. S7 in the Supplemental Material [35]. The atomic scattering factors f_2 for parallel and antiparallel configuration around the Ni L_3-edge, retrieved from XMCD measurements, are shown in blue and green. The voltage optical spectrum is comparable to an XMCD spectrum but instead of having a difference in absorption between parallel and antiparallel orientation of magnetization and photon helicity there is a difference in absorption when applying either a positive or a negative voltage. $\Delta f_{2,V}$ has a maximal negative signal at the onset of the Ni L_3-edge at 849.9 eV. This means that a positive voltage essentially shifts the L_3-edge to slightly higher energies. A positive voltage in the present experimental setup corresponds to an accumulation of holes at the Ni/SiO$_2$ interface. For the Ni atoms, this means that on average they have a slightly higher oxidation number when a positive voltage is applied. Comparison to Ni L_3-edge spectra with different oxidation states shown in [38–40] reveals that the L_3-edge shifts to higher energies for increasing oxidation states of Ni. Hence, the present results show that applying a voltage across the Ni/SiO$_2$ interface leads to a change of the oxidation state of the interfacial

Ni atoms. The difference between a NiO and Ni spectrum is shown in Fig. S8 of the Supplemental Material [35], showing a similar shape as $\Delta f_{2,V}$. This supports the finding of a changed oxidation state due to the applied electric field.

The measurements presented in Figs. 3–5 do not show a significant difference between parallel and antiparallel configuration of magnetization and photon helicity (less than 10%). To obtain good fit results, the same optical properties for parallel and antiparallel configurations are needed; instead, the same values for $\Delta f_{1,V}$ and $\Delta f_{2,V}$ result in good fits for all measurements. This suggests that the states at the Fermi energy populated and depopulated by the applied voltage are either not magnetic or the magnetic component of the voltage optical properties is smaller than the noise level. In other words, the spin polarization at the Fermi energy is rather low at the Ni/SiO$_2$ interface.

Since the resonant intensity of the nonmagnetic L_3-edge $I(f_2)$ is proportional to the number of 3d holes n_d [41,42], the intensity of the voltage x-ray optical property $I(\Delta f_{2,V})$ could be correlated to the change of 3d holes. In the case of Ni, the number of 3d holes is $n_d = 1.66$ in bulk [43]. Hence, the ratio of $I(\Delta f_{2,V})$ to $I(f_2)$ multiplied with n_d represents the measured change of number of holes per Ni atom Δn_d induced by the applied electric field. We can estimate the intensities $I(f_2)$ and $I(\Delta f_{2,V})$ either from the maximum peak heights or by integrating over the spectra, yielding values of $\Delta n_d = 1.14 \times 10^{-3}$ and 1.05×10^{-3}, respectively, resulting in a final value of $(1.10 \pm 0.05) \times 10^{-3}$. This directly corresponds to an averaged interfacial Ni oxidation state change of $(1.10 \pm 0.05) \times 10^{-3}$. The maximum possible change in number of holes per Ni atom $\Delta n_{d,\max}$ can be calculated with the ratio of electrons per area moved by the applied electric field N_{e^-} to the number of interfacial Ni atoms per area affected by the electric field N_{Ni}. N_{e^-} can be calculated from the previously derived effective displacement field D_{rms}, which has a value of $N_{e^-} = D_{\mathrm{rms}} = 4.36 \times 10^{16}$ (e$^-$/m^2) is obtained. The value for N_{Ni} is given by the product of voltage layer width and density. In our simulation, we assumed it to be a Ni monolayer and with the lattice parameter of fcc Ni ($a_0 = 352.4$ pm [44]) we get a value of $N_{\mathrm{Ni}} = 1.61 \times 10^{19}$ (Ni/m^2). With this, the maximum possible change in number of holes per Ni atom $\Delta n_{d,\max}$ takes a value of 2.7×10^{-3} (e$^-$/Ni). This is almost 3 times larger than the ratio of $I(\Delta f_{2,V})$ to $I(f_2)$ obtained above, which suggests that only about 30% of the moving electrons (de-)populate Ni states, and therefore 70% of the electrons have to populate (depopulate) oxygen and silicon states. This conclusion holds up for any choice of N_{Ni} (for details, see Sec. VII, Supplemental Material [35]).

The method of voltage x-ray reflectometry proposed in this study offers exciting new insight into electric field effects at interfaces. This highly sensitive method allows to measure the electric-field-induced variation of reflected x-ray intensity. From those measurements we retrieve a

spectrum of the electric-field-induced changes to the resonant x-ray optical properties at the Ni L_3-edge, which is directly related to the electronic structure. Our results show that the electric field changes the average oxidation state of the interfacial Ni atoms by $(1.1 \pm 0.05) \times 10^{-3}$. Furthermore, we were able to determine that only a thin layer of Ni atoms very close to SiO_2 layer is affected by the applied electric field and determine the position with an accuracy of ± 0.3 nm. Since the x-ray energy can be tuned to various resonant energies this method is not limited to Ni but can be used to study element selective electric-field-induced changes of the electronic structure of interfacial atoms and thus probe states at the Fermi energy. VXRR is a tool that enables quantitative, element specific, and magnetic analysis of buried metal/insulator interfaces and their conduction electrons. This is interesting for the design of spintronic devices, MOSFETs, or capacitors. VXRR could also be used to study ferroelectric systems.

---

[*]Corresponding author.
 e.goering@fkf.mpg.de

[1] W. Kang, L. Chang, Y. Zhang, and W. Zhao, Voltage-controlled MRAM for working memory: Perspectives and challenges, *Proceedings of the 2017 Design, Automation, and Test in Europe DATE 2017* (IEEE, 2017), 542.

[2] T. Nozaki, T. Yamamoto, S. Miwa, M. Tsujikawa, M. Shirai, S. Yuasa, and Y. Suzuki, Recent progress in the voltage-controlled magnetic anisotropy effect and the challenges faced in developing voltage-torque MRAM, Micromachines **10**, 327 (2019).

[3] S. Ikegawa, F. B. Mancoff, J. Janesky, and S. Aggarwal, Magnetoresistive random access memory: Present and future, IEEE Trans. Electron Devices **67**, 1407 (2020).

[4] R. A. One, H. Béa, S. Mican, M. Joldos, P. B. Veiga, B. Dieny, L. D. B. Prejbeanu, and C. Tiusan, Route towards efficient magnetization reversal driven by voltage control of magnetic anisotropy, Sci. Rep. **11**, 8801 (2021).

[5] G. Van Der Laan, Microscopic origin of magnetocrystalline anisotropy in transition metal thin films, J. Phys. Condens. Matter **10**, 3239 (1998).

[6] C. G. Duan, J. P. Velev, R. F. Sabirianov, Z. Zhu, J. Chu, S. S. Jaswal, and E. Y. Tsymbal, Surface Magnetoelectric Effect in Ferromagnetic Metal Films, Phys. Rev. Lett. **101**, 137201 (2008).

[7] K. Nakamura, R. Shimabukuro, Y. Fujiwara, T. Akiyama, T. Ito, and A. J. Freeman, Giant Modification of the Magneto-crystalline Anisotropy in Transition-Metal Monolayers by an External Electric Field, Phys. Rev. Lett. **102**, 187201 (2009).

[8] M. Tsujikawa and T. Oda, Finite Electric Field Effects in the Large Perpendicular Magnetic Anisotropy Surface Pt/Fe/Pt(001): A First-Principles Study, Phys. Rev. Lett. **102**, 247203 (2009).

[9] J. Zhang, P. V. Lukashev, S. S. Jaswal, and E. Y. Tsymbal, Model of orbital populations for voltage-controlled magnetic anisotropy in transition-metal thin films, Phys. Rev. B **96**, 014435 (2017).

[10] P. Bruno, Tight-binding approach to the orbital magnetic moment and magnetocrystalline anisotropy of transition-metal monolayers, Phys. Rev. B **39**, 865 (1989).

[11] S. Miwa, K. Matsuda, K. Tanaka, Y. Kotani, M. Goto, T. Nakamura, and Y. Suzuki, Voltage-controlled magnetic anisotropy in Fe|MgO tunnel junctions studied by x-ray absorption spectroscopy, Appl. Phys. Lett. **107**, 162402 (2015).

[12] T. Kawabe, K. Yoshikawa, M. Tsujikawa, T. Tsukahara, K. Nawaoka, Y. Kotani, K. Toyoki, M. Goto, M. Suzuki, T. Nakamura, M. Shirai, Y. Suzuki, and S. Miwa, Electric-field-induced changes of magnetic moments and magneto-crystalline anisotropy in ultrathin cobalt films, Phys. Rev. B **96**, 220412(R) (2017).

[13] T. Tsukahara, T. Kawabe, K. Shimose, T. Furuta, R. Miyakaze, K. Nawaoka, M. Goto, T. Nozaki, S. Yuasa, Y. Kotani, K. Toyoki, M. Suzuki, T. Nakamura, Y. Suzuki, and S. Miwa, Characterization of the magnetic moments of ultrathin Fe film in an external electric field via high-precision x-ray magnetic circular dichroism spectroscopy, Jpn. J. Appl. Phys. **56**, 060304 (2017).

[14] R. Miyakaze, S. Sakamoto, T. Kawabe, T. Tsukahara, Y. Kotani, K. Toyoki, T. Nakamura, M. Goto, Y. Suzuki, and S. Miwa, Voltage-controlled magnetic anisotropy in an ultrathin nickel film studied by operando x-ray magnetic circular dichroism spectroscopy, Phys. Rev. B **102**, 014419 (2020).

[15] S. Miwa, M. Suzuki, M. Tsujikawa, K. Matsuda, T. Nozaki, K. Tanaka, T. Tsukahara, K. Nawaoka, M. Goto, Y. Kotani, T. Ohkubo, F. Bonell, E. Tamura, K. Hono, T. Nakamura, M. Shirai, S. Yuasa, and Y. Suzuki, Voltage controlled interfacial magnetism through platinum orbits, Nat. Commun. **8**, 15848 (2017).

[16] S. Miwa, M. Suzuki, M. Tsujikawa, T. Nozaki, T. Nakamura, M. Shirai, S. Yuasa, and Y. Suzuki, Perpendicular magnetic anisotropy and its electric-field-induced change at metal-dielectric interfaces, J. Phys. D **52**, 063001 (2019).

[17] S. Macke *et al.*, Element specific monolayer depth profiling, Adv. Mater. **26**, 6554 (2014).

[18] S. Macke and E. Goering, Magnetic reflectometry of heterostructures, J. Phys. Condens. Matter **26**, 363201 (2014).

[19] E. Benckiser, M. W. Haverkort, S. Brück, E. Goering, S. Macke, A. Frañó, X. Yang, O. K. Andersen, G. Cristiani, H. U. Habermeier, A. V. Boris, I. Zegkinoglou, P. Wochner, H. J. Kim, V. Hinkov, and B. Keimer, Orbital reflectometry of oxide heterostructures, Nat. Mater. **10**, 189 (2011).

[20] P. Radhakrishnan, B. Geisler, K. Fürsich, D. Putzky, Y. Wang, S. E. Ilse, G. Christiani, G. Logvenov, P. Wochner, P. A. van Aken, E. Goering, R. Pentcheva, and E. Benckiser, Orbital engineering in YVO_3-$LaAlO_3$ superlattices, Phys. Rev. B **104**, L121102 (2021).

[21] M. Wu, E. Benckiser, P. Audehm, E. Goering, P. Wochner, G. Christiani, G. Logvenov, H. U. Habermeier, and B. Keimer, Orbital reflectometry of $PrNiO_3/PrAlO_3$ superlattices, Phys. Rev. B **91,** 195130 (2015).

[22] E. Benckiser, Y. Khaydukov, L. Guasco, K. Fürsich, P. Radhakrishnan, G. Kim, and B. Keimer, Complementary insights from neutron and resonant X-ray reflectometry for the study of perovskite transition metal oxide heterostructures, Phys. Status Solidi Basic Res. **259,** 2100253 (2022).

[23] S. Brück, G. Schütz, E. Goering, X. Ji, and K. M. Krishnan, Uncompensated Moments in the MnPd/Fe Exchange Bias System, Phys. Rev. Lett. **101,** 126402 (2008).

[24] P. Audehm, M. Schmidt, S. Brück, T. Tietze, J. Gräfe, S. Macke, G. Schütz, and E. Goering, Pinned orbital moments- A new contribution to magnetic anisotropy, Sci. Rep. **6,** 25517 (2016).

[25] J. Geissler, E. Goering, M. Justen, F. Weigand, G. Schütz, J. Langer, D. Schmitz, H. Maletta, and R. Mattheis, Pt magnetization profile in a Pt/Co bilayer studied by resonant magnetic x-ray reflectometry, Phys. Rev. B **65,** 020405(R) (2001).

[26] C. Klewe, T. Kuschel, J. M. Schmalhorst, F. Bertram, O. Kuschel, J. Wollschläger, J. Strempfer, M. Meinert, and G. Reiss, Static magnetic proximity effect in $Pt/Ni_{1-x}Fe_x$ bilayers investigated by x-ray resonant magnetic reflectivity, Phys. Rev. B **93,** 214440 (2016).

[27] O. Inyang, L. Bouchenoire, B. Nicholson, M. Tokaç, R. M. Rowan-Robinson, C. J. Kinane, and A. T. Hindmarch, Threshold interface magnetization required to induce magnetic proximity effect, Phys. Rev. B **100,** 174418 (2019).

[28] A. Moskaltsova, J. Krieft, D. Graulich, T. Matalla-Wagner, and T. Kuschel, Impact of the magnetic proximity effect in Pt on the total magnetic moment of Pt/Co/Ta trilayers studied by X-ray resonant magnetic reflectivity, AIP Adv. **10,** 015154 (2020).

[29] D. Graulich, J. Krieft, A. Moskaltsova, J. Demir, T. Peters, T. Pohlmann, F. Bertram, J. Wollschläger, J. R. Jose, S. Francoual, and T. Kuschel, Quantitative comparison of the magnetic proximity effect in Pt detected by XRMR and XMCD, Appl. Phys. Lett. **118,** 012407 (2021).

[30] A. Verna, P. Alippi, F. Offi, G. Barucca, G. Varvaro, E. Agostinelli, M. Albrecht, B. Rutkowski, A. Ruocco, D. Paoloni, M. Valvidares, and S. Laureti, Disclosing the nature of asymmetric interface magnetism in Co/Pt multilayers, ACS Appl. Mater. Interfaces **14,** 12766 (2022).

[31] D. M. Burn, S. L. Zhang, G. Q. Yu, Y. Guang, H. J. Chen, X. P. Qiu, G. van der Laan, and T. Hesjedal, Depth-Resolved Magnetization Dynamics Revealed by X-Ray Reflectometry Ferromagnetic Resonance, Phys. Rev. Lett. **125,** 137201 (2020).

[32] V. Chardonnet, M. Hennes, R. Jarrier, R. Delaunay, N. Jaouen, M. Kuhlmann, N. Ekanayake, C. Léveillé, C. von Korff Schmising, D. Schick, K. Yao, X. Liu, G. S. Chiuzbăian, J. Lüning, B. Vodungbo, and E. Jal, Toward ultrafast magnetic depth profiling using time-resolved x-ray resonant magnetic reflectivity, Struct. Dyn. **8,** 034305 (2021).

[33] https://www.remagx.org.

[34] S. Brück, S. Bauknecht, B. Ludescher, E. Goering, and G. Schütz, An advanced magnetic reflectometer, Rev. Sci. Instrum. **79,** 083109 (2008).

[35] See Supplemental Material at http://link.aps.org/supplemental/10.1103/PhysRevLett.131.036201 for details about the experimental setup, the error estimation, and complementary data, which includes Ref. [36].

[36] J. Krieft, D. Graulich, A. Moskaltsova, L. Bouchenoire, S. Francoual, and T. Kuschel, Advanced data analysis procedure for hard x-ray resonant magnetic reflectivity discussed for Pt thin film samples of various complexity, J. Phys. D **53,** 375004 (2020).

[37] S. M. Sze and K. K. Ng, *Physics of Semiconductor Devices* (John Wiley and Sons, Ltd, New York, 2006).

[38] H. Wang, C. Y. Ralston, D. S. Patil, R. M. Jones, W. Gu, M. Verhagen, M. Adams, P. Ge, C. Riordan, C. A. Marganian, P. Mascharak, J. Kovacs, C. G. Miller, T. J. Collins, S. Brooker, P. D. Croucher, K. Wang, E. I. Stiefel, and S. P. Cramer, Nickel L-edge soft x-ray spectroscopy of nickel-iron hydrogenases and model compounds—Evidence for high-spin nickel(II) in the active enzyme, J. Am. Chem. Soc. **122,** 10544 (2000).

[39] T. J. Regan, H. Ohldag, C. Stamm, F. Nolting, J. Lüning, J. Stöhr, and R. L. White, Chemical effects at metal/oxide interfaces studied by x-ray-absorption spectroscopy, Phys. Rev. B **64,** 214422 (2001).

[40] H. Wang, D. S. Patil, W. Gu, L. Jacquamet, S. Friedrich, T. Funk, and S. P. Cramer, L-edge X-ray absorption spectroscopy of some Ni enzymes: Probe of Ni electronic structure, J. Electron Spectrosc. Relat. Phenom. **114–116,** 855 (2001).

[41] J. Stöhr and H. C. Siegmann, *Magnetism: From Fundamentals to Nanoscale Dynamics* (Springer, Berlin Heidelberg, 2006), Vol. 152, pp. 1–822.

[42] G. van der Laan, Line shape of 2p magnetic-x-ray-dichroism spectra in 3d metallic systems, Phys. Rev. B **55,** 8086 (1997).

[43] R. Wu and A. J. Freeman, Limitation of the Magnetic-Circular-Dichroism Spin Sum Rule for Transition Metals and Importance of the Magnetic Dipole Term, Phys. Rev. Lett. **73,** 1994 (1994).

[44] T. Nishizawa and K. Ishida, The Co-Ni (Cobalt-Nickel) system, Bull. Alloy Phase Diagrams **4,** 390 (1983).